

Working stroke of the kinesin-14, *ncd*, comprises two substeps of different direction

Bert Nitzsche^{a,b}, Elzbieta Dudek^c, Lukasz Hajdo^c, Andrzej A. Kasprzak^c, Andrej Vilfan^{d,1}, and Stefan Diez^{a,b,1}

^aMax Planck Institute of Molecular Cell Biology and Genetics, 01307 Dresden, Germany; ^bCenter for Molecular Bioengineering (B CUBE), Technische Universität Dresden, 01069 Dresden, Germany; ^cNencki Institute of Experimental Biology, 02-093 Warsaw, Poland; and ^dJ. Stefan Institute, 1000 Ljubljana, Slovenia

Edited by James A. Spudich, Stanford University School of Medicine, Stanford, CA, and approved September 6, 2016 (received for review December 22, 2015)

Single-molecule experiments have been used with great success to explore the mechanochemical cycles of processive motor proteins such as kinesin-1, but it has proven difficult to apply these approaches to nonprocessive motors. Therefore, the mechanochemical cycle of kinesin-14 (*ncd*) is still under debate. Here, we use the readout from the collective activity of multiple motors to derive information about the mechanochemical cycle of individual *ncd* motors. In gliding motility assays we performed 3D imaging based on fluorescence interference contrast microscopy combined with nanometer tracking to simultaneously study the translation and rotation of microtubules. Microtubules gliding on *ncd*-coated surfaces rotated around their longitudinal axes in an [ATP]- and [ADP]-dependent manner. Combined with a simple mechanical model, these observations suggest that the working stroke of *ncd* consists of an initial small movement of its stalk in a lateral direction when ADP is released and a second, main component of the working stroke, in a longitudinal direction upon ATP binding.

kinesin | microtubule | gliding motility assay | fluorescence interference contrast microscopy | mathematical modeling

Single-molecule techniques, in particular single-molecule fluorescence (1) and optical tweezers (2), have greatly advanced our understanding of motor proteins. Such experiments normally rely on the processivity of the motor, which makes it possible to observe multiple consecutive working cycles (i.e., steps). Although single-molecule mechanical measurements on nonprocessive motors can be performed with optical tweezers (3, 4), they require a sophisticated statistical analysis (5, 6) and, if the motor is to be studied under load, advanced feedback (7) or force-clamp mechanisms (8). The minus-end directed C-terminal kinesin-14, *ncd*, is such a nonprocessive motor. It has been shown to play an essential role in spindle focusing (9–11) and to slide and cross-link microtubules (12, 13).

For the working stroke of a single *ncd* motor a lever arm model has been suggested (14, 15). However, as reviewed in ref. 16 the triggering event for the working stroke is still under debate. On the one hand, it has been suggested that the working stroke is connected to the ADP release (14, 17). On the other hand, it has been proposed to be coupled to the binding of ATP to the microtubule (MT)–*ncd* complex (4, 15, 18). In another study, a two-stage displacement of the *ncd* stalk has been proposed where stalk displacement is initiated by binding of *ncd* to the MT and completed upon ATP binding (19). However, even though a variety of approaches including X-ray crystallography (15), EM (20–23), optical trapping (4, 24), FRET (19), and computational modeling (25) have been used to study the coupling between nucleotide states and mechanical states of *ncd*, the exact mechanism remains to be elucidated.

Alternatively, nonprocessive motors can be studied in gliding motility assays (26) albeit with the disadvantage that single-motor behavior is difficult to access. On an *ncd*-coated surface MTs are being translocated with their plus ends leading under the consumption of ATP (27, 28). Remarkably, *ncd* in a gliding motility assay is capable of inducing rotation of MTs in addition to translational movement (28). The reported rotation is right-handed with

a pitch of the order of 300 nm. This value cannot directly be related to the structure of the MT as in the case of kinesin-1, where MT rotation in a gliding motility assay is the result of motors following protofilaments of supertwisted MTs (29). So far it is not clear what exactly governs the rate of MT rotation by *ncd*.

Helical rotation of cytoskeletal filaments by motor proteins has already been observed in a number of cases: (i) rotation of MTs by processive kinesins (30), nonprocessive kinesins (31, 32), and axonemal (33) and cytoplasmic (34) dyneins and (ii) rotation of actin filaments by processive myosins (35, 36), as well as nonprocessive myosins (36, 37). Despite their similarity, the origin of these rotations can be profoundly different. In processive MT motors it can result from side-steps (30, 38, 39), in processive myosins from a mismatch between the actin pitch and the step size (35) and in nonprocessive myosins from the distribution of “target zones” for motor attachment (40). When motors are attached to small beads their relative orientation could also play a role (34), which results in a helicity that varies from bead to bead. None of these mechanisms can explain the rotation of MTs by nonprocessive kinesin, which has to result from an intrinsic property of the motor (i.e., an asymmetric working stroke). The existence of an off-axis component of the stroke has been demonstrated by optical trap experiments (24).

To dissect the working stroke of *ncd* we performed experiments on the collective action of motors by simultaneously measuring the translation and rotation rate in a gliding motility assay. We then fitted the collected data to a simple mechanical model. To address the question what nucleotide state transition the working stroke of *ncd* is coupled to, we varied the kinetics of ATP binding by adjusting the concentration of free ATP and ADP. By comparing the model

Significance

Kinesin, dynein, and myosin motor proteins are best known for their production of linear force along the axes of cytoskeletal filaments. However, many of these motors can also generate torque manifesting itself by filament rotations around their longitudinal axes when gliding on motor-coated surfaces. By combining the measured longitudinal and angular velocities of microtubules gliding on nonprocessive kinesin-14 motors with a theoretical model we here show that the working stroke of this motor comprises at least two distinct conformational changes. Our observations clarify the temporal order of events in the hydrolysis cycle of kinesin-14, which has not been conclusive from previous structural and single-molecule data. Moreover, our results demonstrate how conformational changes in individual enzymes can be deduced from their ensemble properties.

Author contributions: B.N. and S.D. designed research; B.N. performed experiments; E.D., L.H., and A.A.K. contributed new reagents; B.N., A.V., and S.D. analyzed data; A.V. conceived and performed the modelling; and B.N., A.V., and S.D. wrote the paper.

The authors declare no conflict of interest.

This article is a PNAS Direct Submission.

¹To whom correspondence may be addressed. Email: andrej.vilfan@ijs.si or diez@bcube-dresden.de.

This article contains supporting information online at www.pnas.org/lookup/suppl/doi:10.1073/pnas.1525313113/-DCSupplemental.

prediction with the experimental outcome we were able to (i) test the existing models for the triggering event(s) of the ncd working stroke and (ii) draw conclusions on the orientation and magnitude of possible substeps in the working stroke of single ncd motors.

Results

Gliding Motility Assays. To perform gliding motility assays we let GST-tagged ncd (amino acids 195–700) bind specifically to anti-GST IgGs adsorbed to a reflecting silicon surface. Motor densities were kept rather low to prevent potential steric hindrance effects but high enough that MTs were not detaching from the surface during gliding. MTs were assembled in the presence of GMP-CPP [guanylyl-(α,β)-methylene-diphosphonate], thus featuring almost exclusively 14 protofilaments and a supertwist pitch of $8\ \mu\text{M}$ (41, 42). MTs were conjugated with fluorescent quantum dots (QDs) and imaged in gliding motility assays using fluorescence interference contrast (FLIC) microscopy. Combining 2D tracking of xy positions and z information from FLIC intensities we followed the

3D paths of QDs, thereby characterizing the longitudinal and angular motion of MTs as reported previously (42) (Fig. 1A).

MTs rotated in a right-handed fashion when moving forward. Most surprisingly the observed pitch of rotation depended on the ATP concentration ($[\text{ATP}]$) and ranged from 1–2 μm at high $[\text{ATP}]$ to a few hundred nanometers at low $[\text{ATP}]$ (Fig. 1B and C; see also experimental data in Fig. 3). We further measured the longitudinal and angular motion in a buffer containing ADP in addition to ATP. The pitches of rotation became longer with increasing ADP concentration ($[\text{ADP}]$), but the velocities were hardly effected (see experimental data in Fig. S6).

Model. We developed a simple mechanical model that allows us to relate the collective properties of ncd motors in a gliding motility assay to the features of the individual motor molecules. The idea is to use a standard approach (43) for longitudinal motion and extend it in two ways. First, we allow (but do not require) that each change in nucleotide state be coupled to a conformational change.

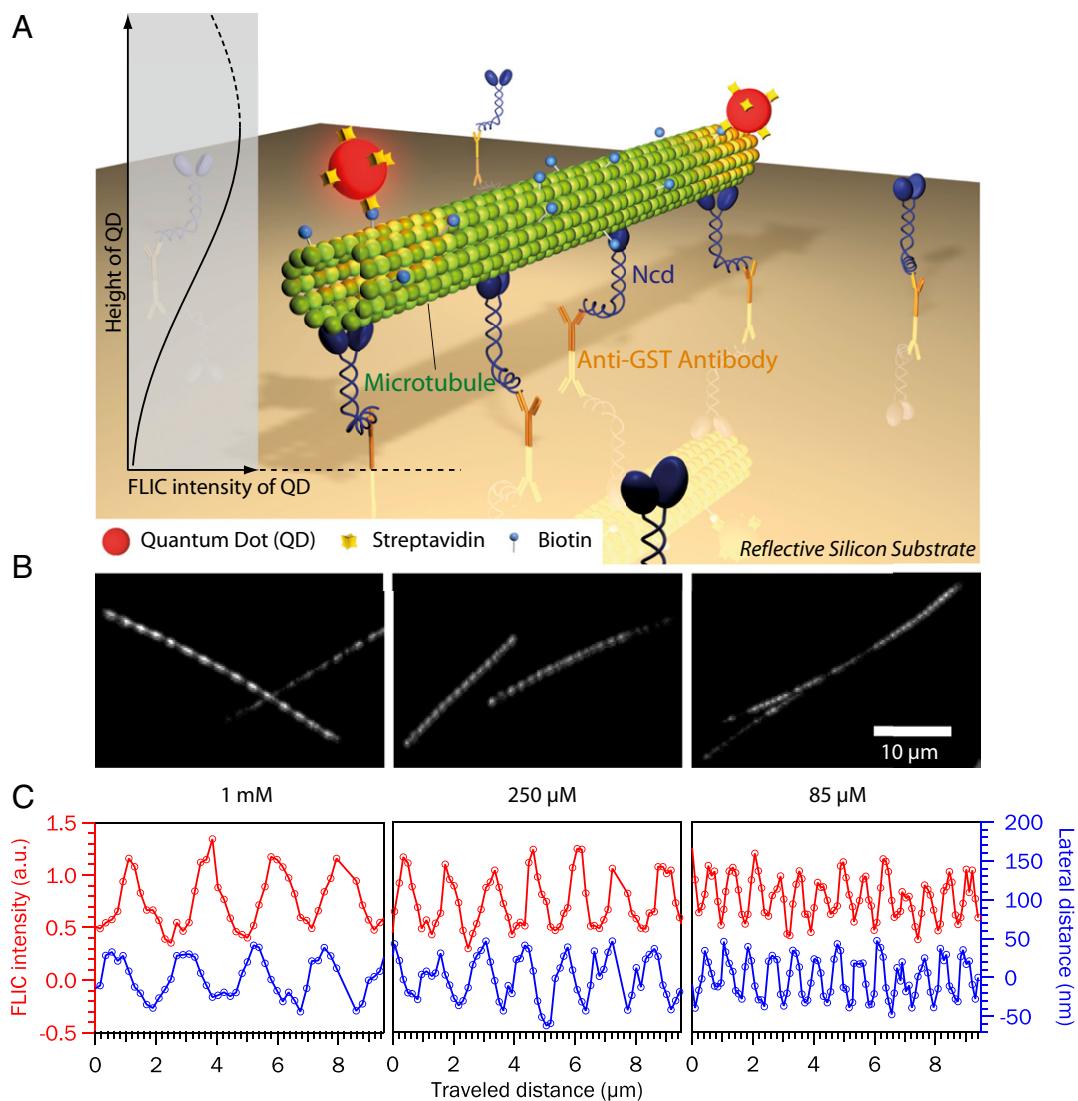


Fig. 1. Measurement of the longitudinal and angular motion of MTs gliding on an ncd-coated surface. (A) Scheme of experimental setup. (B) Maximum intensity projections obtained from time series recordings of QDs attached to MTs gliding on an ncd-coated surface. $[\text{ATP}]$ was 1 mM, 250 μM , and 85 μM (from left to right as indicated). Imaging was performed using FLIC microscopy at frame rates of one per s (for 1 mM and 250 μM) and one per 2 s (for 85 μM). Exposure times were 150 ms. (C) Typical traces of FLIC intensities and lateral deviations of the QD centers from the averaged path—both plotted vs. distance traveled by the MT. Curves correspond to data shown as maximum projections in B. The correlation functions of these traces are described in [Correlation Functions](#) and shown in [Fig. S1](#).

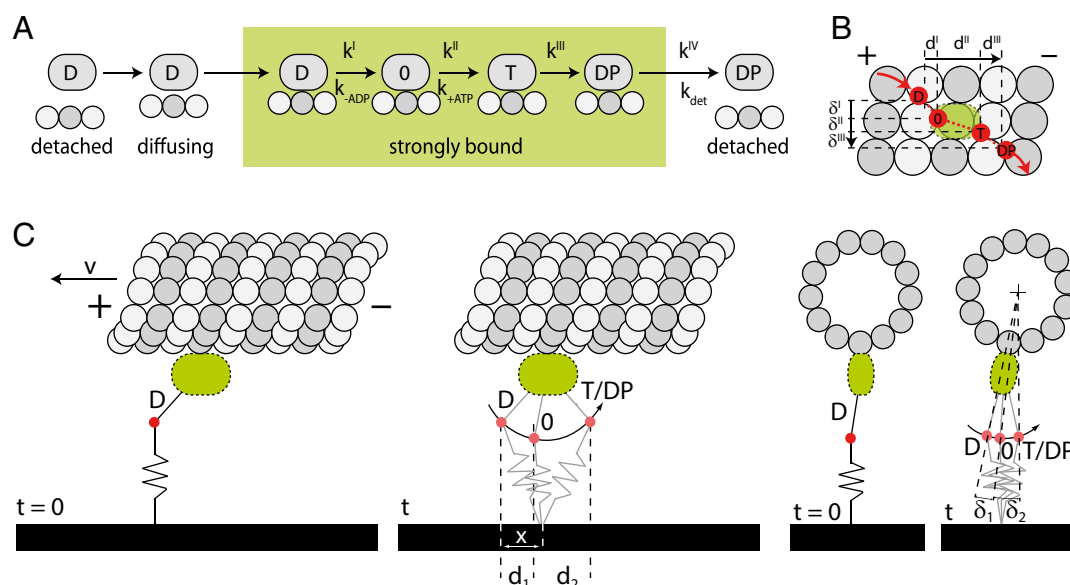


Fig. 2. Hypothetical scheme of the mechanochemical cycle of ncd. (A) MT-binding states (detached, weakly attached/diffusing, and strongly bound) of ncd during its chemical cycle. The chemical states are labeled with D (ADP), O (no nucleotide), T (ATP), and DP (ADP.Pi). (B) Top view: The ncd molecule attaches to the MT in the ADP state and detaches in the ADP.Pi state. During transitions between the strongly bound states ncd potentially undergoes a characteristic longitudinal and angular stalk displacement with respect to the axis of the MT (original stalk position is set to the ADP state). The N-terminal end of the stalk in its different positions is marked by red dots. (C) Schematic representation of ncd in a gliding motility assay immediately after strong binding (*Left*) and some time t later (*Right*) using a reduced kinetic cycle. The lever arm of ncd (stalk) is bound via a flexible attachment to the surface. The working stroke of ncd causes longitudinal (d_1 , d_2) and angular stalk displacements (δ_1 , δ_2 , measured around the MT axis) that strain the connecting spring element and result in a forward force and axial torque on the MT. Simultaneously, MT motion with constant velocity v reduces the spring elongation by the distance $x = vt$. Note that the stalk displacements are effective positions; the distinction between the rigid stalk and the flexible tail has to be viewed as phenomenological.

Second, we not only allow for longitudinal conformational changes but also for orthogonal angular ones. This means that there can be multiple conformational changes per working stroke, each potentially consisting of a longitudinal and an angular component. If the conformational changes have different directions (different ratios between the longitudinal and the angular component), ATP concentration can influence their relative weight in the ensemble and therefore the pitch of MT rotation.

We started by modeling the mechanochemical cycle of a single ncd motor (Fig. 2A) as suggested by previous studies (44–46). The following assumptions represent the generally accepted findings about the mechanochemical cycle of ncd:

- i) The MT-associated state of the motor heads with ADP bound is weakly attached, as evidenced from biochemical studies (46–49) and cryo-EM (18, 22). In fact, it has also been reported that in the presence of ADP ncd motor heads can diffuse along MTs with a diffusion coefficient corresponding to several hundred 8-nm steps in a second (50).
- ii) Upon ADP release ncd enters a strongly bound (rigor) state, thereby getting mechanically coupled to the MT [seen from dissociation constants (51) and EM (15, 18, 22)].
- iii) With ATP bound, ncd remains firmly attached to the MT (15) and detaches after ATP hydrolysis with ADP and P_i bound (52).
- iv) All possible conformational changes are fast and coupled to changes in the nucleotide states of the motor.

For the mechanical model only the states in which the motor is tightly coupled to the MT are relevant—we neglect any forces that the weakly bound motors could exert on the MT. Thus, we only need to consider the part of the mechanochemical cycle that starts with tight binding upon ADP release and ends with detachment of the motor after ATP hydrolysis, but before ADP and P_i release (green box in Fig. 2A). We do not make any a

priori assumptions about the kinetic rates of the different steps in the mechanochemical cycle.

Each of the states listed above is associated with a certain stalk position that is allowed—but not required—to move upon change of the nucleotide state (see top view in Fig. 2B). This way we do not exclude any specific possibility for the mechanochemical cycle. The first possible stalk movement takes place upon ADP release and comprises the longitudinal and angular components, d^I and δ^I . Accordingly, the second shift of the stalk position occurs upon ATP binding and comprises the components d^{II} and δ^{II} . Finally, ATP is hydrolyzed, potentially inducing the conformational changes d^{III} and δ^{III} followed by ncd detachment from the MT. In the following, we will use a reduced kinetic scheme comprising only two steps with the conformational changes d_1 , d_2 and their angular counterparts δ_1 , δ_2 . The reasons are twofold. First, we primarily aim at testing the controversial models in which the working stroke is connected to ADP release, ATP binding, or both events. Second, we obtained very similar results and the same fit quality regardless whether we were using the full or the reduced kinetic scheme.

To derive the gliding velocity and rotational pitch for a MT driven by the collective action of multiple surface-bound ncd motors we assume that the stalk of each ncd is connected with an elastic element (spring constant K) to the glass surface (Fig. 2C). We assume that the filaments do not move sideways, which means that angular displacement of motors translates directly into MT rotation. If the number of motors simultaneously acting on an MT is sufficiently high the gliding velocity v will be constant in time and we can solve the problem by determining the steady-state distribution of motor states and the strains on their elastic elements (simulations described in *Monte-Carlo Simulation* and Fig. S2 show that the approximation is almost exact for ensembles of 20 or more motors). Because the forces acting on motors in a motility assay are relatively low, we assume their effect on the kinetic rates is negligible. The kinetics can then be described with

a simple system of coupled master equations (see Fig. S3 for an example of such a system consisting of four states).

The total force produced by all motors can be expressed as the average number of attached motors $\langle N \rangle$, multiplied by the elastic constant K and the average strain on a motor, $\langle \xi - x \rangle$:

$$F = \langle N \rangle K (\langle \xi \rangle - \langle x \rangle). \quad [1]$$

Here we introduced ξ as the stalk displacement since the initial binding (Fig. S4A). In our reduced two-step model the values $\xi = d_1$ in state 1 and $\xi = d_1 + d_2$ in state 2 are possible. x is defined as the displacement of the MT due to gliding motion, measured from initial binding (Fig. 2C and Fig. S4A). The brackets $\langle \rangle$ denote ensemble averaging among all bound motors.

The average stalk displacement $\langle \xi \rangle$ of all bound motors is obtained by averaging stalk displacements (d_1 and $d_1 + d_2$) weighted by the fraction of time an attached motor dwells in state i ($\tau_i / \sum_j \tau_j$),

$$\langle \xi \rangle = d_1 \frac{\tau_1}{\tau_1 + \tau_2} + (d_1 + d_2) \frac{\tau_2}{\tau_1 + \tau_2}. \quad [2]$$

τ_1 and τ_2 , the average dwell times in state 1 (no nucleotide) and state 2 (ATP), are related to the kinetic rates as

$$\tau_1 = \frac{1}{k_{+ATP}[ATP]} \quad \tau_2 = \frac{1}{k_{det}}. \quad [3]$$

Two examples of the distributions $P(\xi)$ for different ATP concentrations are shown in Fig. S4C.

In Eq. 1, $\langle x \rangle$ is the average MT displacement between initial binding and the point of observation. For gliding motion with a constant velocity v it equals $\langle vt \rangle$, where t is the time since initial attachment. It can be evaluated as

$$\langle t \rangle = \frac{\int_0^\infty S(t)t dt}{\int_0^\infty S(t)dt}, \quad [4]$$

where $S(t)$ is the probability that the motor is still attached at time t after the initial strong binding (“survival function” of the bound state, Fig. S4B). In a model with two bound states the contribution of state 1 to the integral in the numerator is τ_1^2 and that of the second state $\tau_2(\tau_1 + \tau_2)$. The denominator is simply the average dwell time in the attached state. We therefore obtain

$$\langle x \rangle = v \frac{\tau_1^2 + (\tau_1 + \tau_2)\tau_2}{\tau_1 + \tau_2}. \quad [5]$$

Two examples of the probability distributions $P(x)$ are shown in Fig. S4C. A general discussion of the expression for $\langle x \rangle$ in a system with more states is given in *Distribution of States After Strong Binding*.

In a gliding motility assay force equilibrium states $F = 0$ and therefore (Eq. 1) $\langle \xi \rangle = \langle x \rangle$. Inserting Eqs. 2 and 5 into this condition we obtain an expression for the gliding velocity

$$v = \frac{d_1 \tau_1 + (d_1 + d_2)\tau_2}{\tau_1^2 + (\tau_1 + \tau_2)\tau_2}. \quad [6]$$

An analogous calculation for the angular velocity yields

$$\omega = \frac{\delta_1 \tau_1 + (\delta_1 + \delta_2)\tau_2}{\tau_1^2 + (\tau_1 + \tau_2)\tau_2}. \quad [7]$$

Finally, the pitch of rotation is defined as

$$\lambda = \frac{2\pi v}{\omega}. \quad [8]$$

An alternative derivation of Eq. 6, following the approach of master equations, is given in *Alternative Solution* and Fig. S5. In addition, the results are supported by a Monte-Carlo simulation (*Monte-Carlo Simulation*).

For a motor with a single rate limiting step (e.g., $d_1 = 0$, $\tau_1 = 0$), the velocity (Eq. 6) simplifies to the well-known expression $v = d/\tau$, which is frequently used to interpret myosin velocities (53). If there are two rate-limiting steps, the result becomes strongly dependent on the order of events. If the working stroke takes place before the ATP waiting state ($d_1 > 0$, $d_2 = 0$), the resulting velocity as a function of [ATP] already has a different dependence than the ATPase rate, which follows Michaelis–Menten kinetics. Leibler and Huse (43) found that for myosin the velocity as a function of [ATP] does not exactly follow the Michaelis–Menten law, but the deviation from the Michaelis–Menten law is small (they call it “Michaelis-like law”). If, however, the waiting state precedes the working stroke ($d_1 = 0$, $d_2 > 0$), the dependence $v([ATP])$ becomes quadratic at low ATP concentrations. Although the total working stroke is the same, heads spend the longest part of the cycle in the prestroke state and therefore contribute little to the forward motion. If there are two

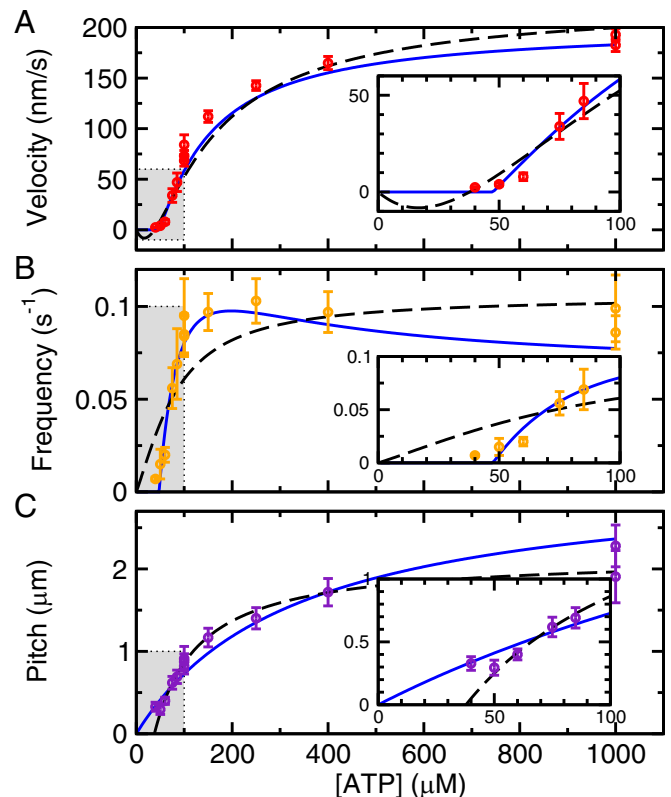


Fig. 3. Dependence of motility of gliding MTs on [ATP]—comparison between experimental data and model. (A) longitudinal velocity, (B) angular frequency, and (C) pitch of rotation. Individual points represent experimental data (mean values derived from full rotations \pm SDs. All data displayed are from the same gliding assay where imaging was performed in a constant field of view to keep conditions stable. ATP concentration was consecutively reduced from initial 1 mM down to 40 μ M. To exclude artifacts due to aging of the sample control measurements at 1 mM and 100 μ M [ATP] were performed after a complete dataset had been acquired. Fits: Dashed lines in A and C represent the fit using the basic version of the model (Eqs. 6–8) and continuous blue lines the model version including friction and the ADP data set (see Fig. S6 for full dataset). The curves in B were not fitted separately but obtained by using Eq. 8 with the fits from A and C.

substeps of opposite direction ($d_1 < 0$, $d_2 > 0$), a velocity reversal depending on the ATP concentration is theoretically possible (54).

Fitting Procedure. To test whether our model correctly describes the properties of MTs gliding on an ncd-coated surface we extracted gliding velocities, rotation frequencies, and pitches from gliding motility assays as described above (Fig. 1) and fitted our model (Fig. 3, dashed lines). Note that the parameters of this model (six in total) cannot be determined from v and ω alone. We therefore use a result obtained with optical tweezers (4), which measured a total displacement $d_1 + d_2 = 9$ nm. We do not make any other assumption about the model parameters. The fitting procedure then involves five parameters to fit two sets of data (gliding velocity and pitch of rotation).

Although overall the model fits the data well, there are small discrepancies at low [ATP] (below 100 μ M), where the model fails to fit the sharp drop in velocity. Either the model predicts a reversal of direction at a certain [ATP], which is not observed experimentally, or—if we impose $d_1 = 0$ —a quadratic dependence of gliding velocity on [ATP]. The actually measured dependence of gliding velocity on [ATP] is flatter at low concentrations and steeper above the threshold. We therefore extended the model by including a parameter for passive friction that acts on the filament in addition to the active motors.

Model with Friction. Because we found that the gliding velocity does not depend on MT length, we conclude that the friction force has the same length dependence as the pulling force induced by the motors, whose number scales linearly with MT length. Considering the possibility that part of the motors have restricted activity (inactive or sticky motors) this approach is reasonable.

We thus introduce the parameter f denoting the friction force per active motor if the filament is moving. Thereby, we model friction in a completely phenomenological way and assume that the friction force is constant—independent of velocity. When the filament is stalled the friction per motor can have any value between 0 and f . The friction force has to counterbalance the total force produced by the motors, Eq. 1,

$$f = \frac{\tau_1 + \tau_2}{\tau_{\text{off}} + \tau_1 + \tau_2} K \left(\frac{d_1 \tau_1 + (d_1 + d_2) \tau_2}{\tau_1 + \tau_2} - v \frac{\tau_1^2 + \tau_1 \tau_2 + \tau_2^2}{\tau_1 + \tau_2} \right). \quad [9]$$

Here we introduced τ_{off} as the average time the motor spends in the detached or weakly bound state. The fraction of bound motors is then determined as the average time in the strongly bound state ($\tau_1 + \tau_2$), divided by the total cycle time ($\tau_{\text{off}} + \tau_1 + \tau_2$). The velocity v follows as

Table 1. Fit parameters of the model (mean, 95% confidence interval)

Model	Without friction	With friction
d_1 , nm	-3.8 [-5.2, -2.4]	0*
$d_1 + d_2$, nm	9^\dagger	9^\dagger
δ_1 , °	0.93 [-0.02, 1.88]	6.36 [3.99, 8.73]
$\delta_1 + \delta_2$, °	1.50 [0.86, 2.14]	1.03 [0.79, 1.27]
$k_{+\text{ATP}}$, $\mu\text{M}^{-1}\cdot\text{s}^{-1}$	0.28 [0.21, 0.35]	0.79 [0.44, 1.14]
k_{detr} , s^{-1}	25 [22, 28]	42 [37, 48]
f/K , nm		4.2 [3.4, 5.0]
$k_{+\text{ADP}}$, $\mu\text{M}^{-1}\cdot\text{s}^{-1}$		0.030 [0.017, 0.043]

*No improvement of the fit with a finite value.

† From ref. 4.

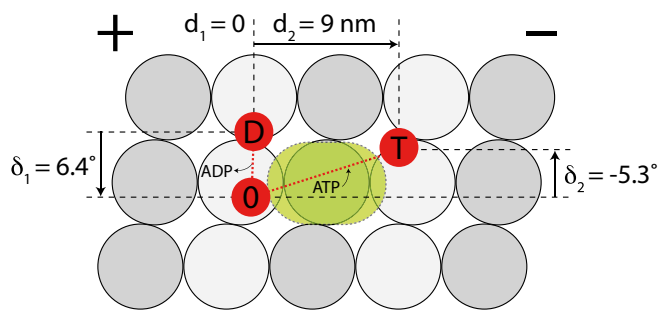


Fig. 4. Longitudinal and angular components of neck displacement before and after binding of ATP; values are based on the model including friction (not drawn to scale).

$$v = \frac{d_1 \tau_1 + (d_1 + d_2) \tau_2 - \frac{f}{K} (\tau_{\text{off}} + \tau_1 + \tau_2)}{\tau_1 (\tau_1 + \tau_2) + \tau_2^2}. \quad [10]$$

This expression holds as long as the numerator is positive—otherwise the solution is $v = 0$.

From the nature of a friction force we estimate that it reduces the longitudinal and the angular motion by the same fraction. The pitch, determined by their ratio, then remains the same as in the model without friction (Eq. 8), which is

$$\lambda = 2\pi \frac{d_1 \tau_1 + (d_1 + d_2) \tau_2}{\delta_1 \tau_1 + (\delta_1 + \delta_2) \tau_2}. \quad [11]$$

The model fit with friction took into account data in the presence of ADP to avoid overfitting the model. The resulting fits are shown by the continuous lines in Fig. 3. Fit quality is noticeably better than for the simple version of the model.

A direct result of the fitting procedure are the values of the working stroke components that are represented by the fit parameters (Table 1). Fig. 4 shows the values of substeps in the working stroke for the model including friction. When ncd binds to the MT and ADP is being released the stalk is only displaced laterally, causing angular MT displacement of 6.4° . When ATP binds, an angular displacement by 5.3° in the opposite direction is accompanied by a longitudinal stalk displacement of 9 nm, which can be regarded as the main working stroke of ncd.

The model can be extended to calculate the velocity and pitch in the presence of ADP, along with ATP. We expect that ADP in solution can lead to the reversal of the initial weak-to-strong binding transition and extend the kinetic scheme from Fig. 2 accordingly. All model calculations involving ADP are presented in *Model Taking into Account the Presence of ADP*. Generally, the pitch increases with ADP concentration, as we see in our experiments. The velocity is less influenced by ADP. Some increase could be caused by ADP unblocking the inactive motors and thus reducing friction.

Discussion

We showed that the working stroke of ncd consists of two substeps with different directions. The first substep is angular in direction (i.e., off-axis) and occurs when ADP unbinds during the formation of the ncd-MT complex. The second and by amplitude main substep occurs when ATP binds to the ncd-MT complex.

Our results are in line with evidence from cryo-EM studies (15, 18) showing a large-scale rotation of the unbound motor domain of ncd-MT complexes in the presence of adenylyl-imidodiphosphate (AMP-PNP) (mimicking the ATP-bound state) compared with the conformation in the absence of nucleotide. Endres et al. (15) could even explicitly visualize a neck rotation of $\approx 70^\circ$ toward the minus end of the MT in the presence of AMP-PNP in their EM density

maps. In addition, both reports (15, 18) find that MT-bound ncd in the absence of nucleotide closely resembles the structure of ncd in the ADP state known from X-ray crystallography. In summary, structural studies that addressed the nature of the working stroke of ncd argue for the main working stroke to happen upon ATP binding. At the same time the data from these studies indicate that if there is a stalk movement upon ADP release it has to be very small. Our data, providing strong evidence for a two-step displacement of the stalk when ncd is going through its mechanochemical cycle, add to this picture. Without having to rely on exact numbers for directions and amplitudes of the displacements this can directly be deduced from Eqs. 8 and 11 (here summarized as Eq. 12):

$$\lambda = \frac{2\pi v}{\omega} = 2\pi \frac{d_1 k_{\text{det}} + (d_1 + d_2) k_{+\text{ATP}} [\text{ATP}]}{\delta_1 k_{\text{det}} + (\delta_1 + \delta_2) k_{+\text{ATP}} [\text{ATP}]} \quad [12]$$

The equations are valid for both versions of our model with and without friction (i.e., independent of the friction component introduced in the extended version of the model).

We have shown that our model adequately describes the dependence of v , λ , and thus ω on [ATP]. In particular it is interesting that λ increases as [ATP] is increasing. What does this [ATP]-dependent pitch of rotation (Eq. 12) mean for the possible working stroke components of ncd? The case $d_1 = 0$ and $\delta_1 = 0$ would correspond to the working stroke taking place exclusively upon ATP binding. Likewise the case $d_2 = 0$ and $\delta_2 = 0$ would correspond to the working stroke taking place exclusively upon ADP release. For both cases, our model would predict the pitch λ to be independent of [ATP]. This is incompatible with our experimental data. In contrast, λ becomes a function of [ATP] if the condition $d_1/\delta_1 \neq d_2/\delta_2$ is fulfilled. Therefore, our experimental data provide strong evidence that the working stroke comprises two parts, where the first one is triggered by ADP release and the second one by ATP binding. In particular, the directions of these substeps in the working stroke must be different from each other because identical directions would mean $d_1/\delta_1 = d_2/\delta_2 = \lambda/2\pi$, where λ would not depend on the ATP concentration.

Beyond these qualitative considerations, quantitative fitting of the parameters of our model helped to resolve the working stroke of ncd in more detail than previously known. Earlier experiments measuring the mechanochemical cycle of ncd based on optical tweezers showed a two-stage process with binding of ncd to the MT and subsequent working stroke (4). The binding was associated with an initial small off-axis displacement that was attributed to an artifact because of the experimental geometry. The off-axis component that we found for the first part of the working stroke may provide an alternative explanation for this observation. The strength of our method working with large ensembles of motors in a motility assay becomes evident here.

Similar to our results a recent publication (19) suggests a two-step displacement of the stalk—the first one upon ncd binding to the MT and a second one upon binding of ATP to the MT-bound motor domain. However, unlike our considerations, that study treats the two substeps as parts of one large displacement in a single plane without giving information on how the magnitudes of the substeps relate to each other.

The substep of the working stroke that takes place upon ATP binding is also directly linked to the shape of the velocity curve at low [ATP]. Because the ATP-waiting state takes place before the working stroke, ATP concentration affects the fraction of time the motor dwells in the pre- and the postworking stroke state. Here, we found that at low [ATP] the MT velocities were dropping more abruptly than one would expect if the velocity was directly proportional to the ATPase rate that follows the Michaelis–Menten kinetics (Fig. 3). Interestingly, even our basic model

without friction extension reproduces this effect at least partly. Although the ATPase rate in the model follows the Michaelis–Menten law, the predicted velocity (Eq. 6) and rotation frequency (Eq. 7) do not. An unconstrained fit also gives a negative initial working stroke ($d_1 < 0$) and, as a consequence, a small range of ATP concentrations with reverse velocities. A negative working stroke could be consistent with single-molecule observations that show a fraction of negative (plus-end-directed) displacements (6). We never observed negative velocities, however. The extended model fits the non-Michaelis–Menten shape of the velocity curve even better, suggesting that friction might be contributing to the effect. Unlike the present experiments a previous report by deCastro et al. (55) shows MT velocities that follow Michaelis–Menten dependence. We do not have an explanation for this discrepancy, although a different fraction of inactive motors could play a role.

We explicitly note that our findings are not based on previously measured kinetic rates of ncd. Although we used one mechanical parameter (total working stroke size) from the literature, we obtained all kinetic parameters by fitting and can compare them with values from solution kinetics. The value of $k_{+\text{ATP}}$ we obtain is $0.3 \mu\text{M}^{-1}\cdot\text{s}^{-1}$ and $0.8 \mu\text{M}^{-1}\cdot\text{s}^{-1}$ in the model without and with friction, respectively. In comparison, direct kinetic measurements give the values $1.5 \mu\text{M}^{-1}\cdot\text{s}^{-1}$ (47), $2 \mu\text{M}^{-1}\cdot\text{s}^{-1}$ (46), $0.057 \mu\text{M}^{-1}\cdot\text{s}^{-1}$ [effective value, calculated from steady-state ATPase (45)], and $1.06 \mu\text{M}^{-1}\cdot\text{s}^{-1}$ [with mantATP (45)]. For the detachment rate after the binding of ATP (k_{det}) we obtain 25 s^{-1} (without friction) and 42 s^{-1} (with friction). Comparable kinetic results are 14 s^{-1} (45). The detachment rate upon ADP binding is an effective rate that replaces two consecutive steps and is therefore not directly comparable. Overall, kinetic parameters obtained from our model match previously published measurements quite well.

In conclusion, we have developed an approach to derive information about single nonprocessive motor proteins from their collective action. This can be helpful in cases where the action of single molecules cannot be measured with sufficient resolution or is not accessible at all. Specifically, we have characterized the working stroke of ncd in more detail. We provide evidence for an initial small movement of the ncd stalk in an angular direction when ADP is released and a second, main component of the working stroke in a longitudinal direction when ATP is binding to the MT-bound motor domain.

Materials and Methods

Buffers. Three types of Hepes-based buffer solutions were used for purification of ncd and to prepare solutions for the different incubation steps when preparing in vitro gliding motility assays: (i) SB10 (sample buffer 10) consisting of 10 mM Hepes (Roth), pH 7.3 adjusted using NaOH (Merck), 1 mM EGTA, and 1 mM MgCl_2 ; (ii) SB50 (sample buffer 50), identical to SB10 except for Hepes concentration, which was 50 mM; and (iii) SB50+ (sample buffer 50+), SB50 augmented with 100 mM NaCl (Merck/VWR), 1 μM taxol (Sigma-Aldrich), 0.2 $\text{mg}\cdot\text{mL}^{-1}$ casein (Sigma-Aldrich), 10 mM DTT, 2 mM Trolox (Fluka), 5 mM PCA (Sigma-Aldrich), and NaOH (to readjust pH to 7.3).

Kinesin-14 Protein. All experiments were performed using a GST-ncd^{195–700} where the WT fragment encoding for amino acids 195–700 of ncd was cloned into a pGEX4T1 vector. The construct was purified based on a procedure reported previously (56). The salt concentration for elution of the GST-ncd^{195–700} had been determined by salt gradient FPLC before.

Ncd was expressed in *Escherichia coli* BL21 pRARE induced by 0.5 mM isopropyl- β -D-thiogalactopyranoside. After 16 h at 15 °C bacteria were harvested by centrifugation at $8,000 \times g$ and 4 °C for 10 min. The pellet was resuspended at 1 $\text{g}\cdot\text{mL}^{-1}$ in SB10, snap-frozen in liquid nitrogen, and stored at -80 °C. For purification the bacterial pellet was thawed and diluted in buffer A [SB10 augmented with 50 mM NaCl, protein inhibitor mix (1 mM PMSF, 1 $\mu\text{g}\cdot\text{mL}^{-1}$ leupeptin, 1 $\mu\text{g}\cdot\text{mL}^{-1}$ pepstatin A, 2 $\mu\text{g}\cdot\text{mL}^{-1}$ aprotinin, and 2 $\mu\text{g}\cdot\text{mL}^{-1}$ $\text{N}\alpha$ -*p*-Tosyl-L-arginine methyl ester hydrochloride, all from Sigma-Aldrich), 0.5 mM DTT, 50 μM ATP, and 12.5 U/mL Benzonase (Novagen). Cells were lysed using an EmulsiFlex-C5 high-pressure homogenizer (Avestin). Lysate was centrifuged at $25,000 \times g$ for 30 min. Supernatant was spun again at $140,000 \times g$ for 2 h. The remaining supernatant was loaded onto an

SP-Sepharose column (GE Healthcare) coupled to a peristaltic pump. The column was then washed with buffer A and subsequently eluted using buffer B (identical to buffer A except for 250 mM NaCl instead of 50 mM NaCl). Flow rates were about 1 mL·min⁻¹ except for elution, which was done at about 0.5 mL·min⁻¹. Fractions containing the eluate were augmented with 10% (wt/vol) sucrose. After subsequent centrifugation at 100,000 × *g* and 4 °C for 20 min supernatant was snap-frozen and stored in liquid nitrogen.

MTs. Using a mix of 98% unlabeled, 1% rhodamine-labeled, and 1% biotinylated bovine tubulin (all from Cytoskeleton Inc.) MTs were assembled as previously described (42). One hundred microliters of a 2 μM tubulin-containing solution consisting of BRB80 [80 mM Pipes (Sigma), pH 6.9, with KOH (VWR), 1 mM EGTA (Sigma), and 1 mM MgCl₂ (VWR)], 1 mM GMP-CPP (Jena Bioscience), and 4 mM MgCl₂ were incubated for 2 h at 37 °C. MTs were sedimented at 100,000 × *g* for 5 min using a Beckman Airfuge. The pellet was resuspended in a volume of 50 μL BRB80 supplemented by 10 μM taxol (Sigma).

In Vitro Gliding Motility Assays. Gliding motility assays were performed in flow chambers as described previously (57). In short, a flow chamber was assembled from a PEG-functionalized 22- × 22-mm coverslip and a 10- × 10-mm Si chip featuring an oxide layer of about 30 nm coated with dichlorodimethylsilane (Sigma-Aldrich) using a coating procedure described previously (58). Spacers of NESCO film were placed such that the resulting channels were 10 mm × 1.5 mm × 100 μm.

Five microliters of anti-GST antibodies (clone: S-tag-05; antibodies-online GmbH) were perfused into the flow chamber at 0.02 mg·mL⁻¹ (1:50 diluted in PBS) and allowed to adsorb to the surface for 2 min. Then the surface was blocked by perfusion of 10 μL Pluronic F127 (Sigma P2443, 1% in PBS and 0.2-μm filtered). After 15 min Pluronic F127 was removed by four washing steps with 10 μL solution each of (i) 2 × 10 μL PBS and (ii) 2 × 10 μL SB10, pH 7.3, and 100 mM NaCl. Next, 5 μL of 3 μM GST-ncd^{195–700} in SB10 augmented with 100 mM NaCl, 0.2 mg·mL⁻¹ casein, 100 μM ATP, and 10 mM DTT was perfused into the flow chamber at concentrations ranging from and allowed to bind to the antibodies for 10 min. Unbound motor was removed by washing the flow chamber with 4 × 10 μL SB50 augmented with 100 mM NaCl, 0.2 mg·mL⁻¹ casein, 100 μM ATP, and 10 mM DTT. MTs in SB50+ containing 1 mM ATP were perfused into the flow chamber and replaced after 10 min by a QD-containing solution composed of SB50+, 100 pM Q655 (Q10121MP; Molecular Probes), and 1 mM ATP. After incubation for 10 min unbound QDs were removed by imaging solution composed of SB50+, 1 mM ATP, and 50 nM PCD (protocatechuate 3,4-dioxygenase from *Pseudomonas* sp.; Sigma-Aldrich). This imaging buffer with variable ATP concentrations ranging from 40 μM to 1 mM (and for the ADP experiments ADP concentrations up to 1 mM) was perfused into the flow chamber to adjust ATP concentration during the experiment. Temperature was kept at 22 °C during imaging. Whenever solutions in the flow chamber were exchanged in the course of the imaging process, sample illumination was interrupted to prevent phototoxic effects on the sample.

Optical Imaging. An inverted fluorescence microscope (Axiovert 200M; Zeiss) equipped with a 63× water immersion 1.2 N.A. objective (Zeiss) and an Andor Ixon DV 897 (Andor) electron-multiplying CCD camera was used for image acquisition. Fluorescence excitation was achieved using a liquid-waveguide coupled Lumen 200 metal arc lamp (Prior Scientific Instruments Ltd.). Specific filter sets were used for imaging of QDs Q655 and TAMRA-labeled MTs: Q655: exc 475/42 (Semrock), dc BS 517 imaging, em 655/40 and TAMRA exc HQ 535/50, dc Q 565 LP, em HQ 610/75 (Chroma Technology). Time-series movies of the QDs were recorded at rates ranging from 0.1 to 1 frames per s (fps) (0.1 fps for the lowest ATP concentrations, 0.25 fps above 60 μM, 0.5 fps above 85 μM, and 1 fps above 150 μM). Every 50 frames a TRITC image was recorded to check the MTs. Exposure time was 150 ms.

Data Analysis. Positions of QD images were determined using in-house software for single-particle tracking (59) based on MATLAB (MathWorks). Postprocessing of these data was performed using MATLAB and Igor Pro v6. Pitches of rotation were determined according to the maxima and minima of the FLIC intensity curves of MT-attached QDs complemented by the corresponding curves showing the distance between the QD positions from the MT trajectory (positive displacement corresponds to displacement to the left when looking in the direction of motion). The MT trajectory was approximated by sliding window averaging of QD positions. The values were verified by cross-correlating the FLIC intensity curve and *xy*-deviation curve (*Correlation Functions*).

Fitting. In the model without friction we applied a global fit of Eq. 6 for the velocity and Eqs. 6–8 for the helical pitch data. We fixed the value of $d_1 + d_2$ and fitted the remaining five parameters: k_{+ATP} , k_{det} , d_1 , δ_1 , and δ_2 . The data were fitted with the least squares method weighted with the inverse square of the SE. The SE of parameters was estimated as square root of the diagonal elements of the variance-covariance matrix (Numerical Algorithms Group routines E04FFY and E04YCF) and the 95% confidence intervals as mean ± 1.96 SE. The rotation frequency was derived from the velocity and helical pitch data through Eq. 8.

When applying the model with friction to the data we fitted globally (i) the velocity data with different ATP concentrations in the absence of ADP and (ii) the pitch at different ATP and ADP concentrations. Again, we used the weighted least-squares fitting procedure. This way we determined the model parameters k_{+ATP} , k_{det} , δ_1 , δ_2 , f/K , and k_{+ADP} . We set $d_1 = 0$ because allowing a nonzero value led to no improvement of the fit quality. With these parameters we further calculated the velocity for different ADP concentrations and finally the rotation frequency through Eq. 8. A sensitivity analysis of the fitting results to the parameters d_1 , $d_1 + d_2$, τ_{off} , and γ is shown in *Sensitivity Analysis* and Fig. S7.

ACKNOWLEDGMENTS. We thank Corina Bräuer and Franziska Friedrich for technical support, Lennart Hilbert for comments on the manuscript, and Sharyn Endow for support during the early stage of the project. This work was supported by European Research Council Starting Grant 242933 (NanoTrans), German Research Foundation Heisenberg Programme Grant DI 1226/4, and Slovenian Research Agency Grant P1-0099.

- Yildiz A, Tomishige M, Vale RD, Selvin PR (2004) Kinesin walks hand-over-hand. *Science* 303(5658):676–678.
- Svoboda K, Schmidt CF, Schnapp BJ, Block SM (1993) Direct observation of kinesin stepping by optical trapping interferometry. *Nature* 365(6448):721–727.
- Finer JT, Simmons RM, Spudis JA (1994) Single myosin molecule mechanics: Piconewton forces and nanometre steps. *Nature* 368(6467):113–119.
- deCastro MJ, Fondecave RM, Clarke LA, Schmidt CF, Stewart RJ (2000) Working strokes by single molecules of the kinesin-related microtubule motor ncd. *Nat Cell Biol* 2(10):724–729.
- Smith DA, Steffen W, Simmons RM, Sleep J (2001) Hidden-Markov methods for the analysis of single-molecule actomyosin displacement data: The variance-Hidden-Markov method. *Biophys J* 81(5):2795–2816.
- Butterfield AE, Stewart RJ, Schmidt CF, Skliar M (2010) Bidirectional power stroke by ncd kinesin. *Biophys J* 99(12):3905–3915.
- Veigel C, Molloy JE, Schmitz S, Kendrick-Jones J (2003) Load-dependent kinetics of force production by smooth muscle myosin measured with optical tweezers. *Nat Cell Biol* 5(11):980–986.
- Capitanio M, et al. (2012) Ultrafast force-clamp spectroscopy of single molecules reveals load dependence of myosin working stroke. *Nat Methods* 9(10):1013–1019.
- Endow SA, Chandra R, Komma DJ, Yamamoto AH, Salmon ED (1994) Mutants of the *Drosophila* ncd microtubule motor protein cause centrosomal and spindle pole defects in mitosis. *J Cell Sci* 107(Pt 4):859–867.
- Goshima G, Nédélec F, Vale RD (2005) Mechanisms for focusing mitotic spindle poles by minus end-directed motor proteins. *J Cell Biol* 171(2):229–240.
- Cross RA, McAlinsh A (2014) Prime movers: The mechanochemistry of mitotic kinesins. *Nat Rev Mol Cell Biol* 15(4):257–271.
- Oladipo A, Cowan A, Rodionov V (2007) Microtubule motor Ncd induces sliding of microtubules in vivo. *Mol Biol Cell* 18(9):3601–3606.
- Fink G, et al. (2009) The mitotic kinesin-14 Ncd drives directional microtubule-microtubule sliding. *Nat Cell Biol* 11(6):717–723.
- Yun M, et al. (2003) Rotation of the stalk/neck and one head in a new crystal structure of the kinesin motor protein, Ncd. *EMBO J* 22(20):5382–5389.
- Endres NF, Yoshioka C, Milligan RA, Vale RD (2006) A lever-arm rotation drives motility of the minus-end-directed kinesin Ncd. *Nature* 439(7078):875–878.
- Cross RA (2010) Kinesin-14: The roots of reversal. *BMC Biol* 8:107.
- Heuston E, Bronner CE, Kull FJ, Endow SA (2010) A kinesin motor in a force-producing conformation. *BMC Struct Biol* 10:19.
- Wendt TG, et al. (2002) Microscopic evidence for a minus-end-directed power stroke in the kinesin motor ncd. *EMBO J* 21(22):5969–5978.
- Hallen MA, Liang ZY, Endow SA (2011) Two-state displacement by the kinesin-14 Ncd stalk. *Biophys Chem* 154(2-3):56–65.
- Sosa H, et al. (1997) A model for the microtubule-Ncd motor protein complex obtained by cryo-electron microscopy and image analysis. *Cell* 90(2):217–224.
- Sosa H, Milligan RA (1996) Three-dimensional structure of ncd-decorated microtubules obtained by a back-projection method. *J Mol Biol* 260(5):743–755.
- Hirose K, Cross RA, Amos LA (1998) Nucleotide-dependent structural changes in dimeric NCD molecules complexed to microtubules. *J Mol Biol* 278(2):389–400.
- Hirose K, Löwe J, Alonso M, Cross RA, Amos LA (1999) Congruent docking of dimeric kinesin and ncd into three-dimensional electron cryomicroscopy maps of microtubule-motor ADP complexes. *Mol Biol Cell* 10(6):2063–2074.
- Endow SA, Higuchi H (2000) A mutant of the motor protein kinesin that moves in both directions on microtubules. *Nature* 406(6798):913–916.
- Jana B, Hyeon C, Onuchic JN (2012) The origin of minus-end directionality and mechanochemistry of Ncd motors. *PLOS Comput Biol* 8(11):e1002783.

26. Toyoshima YY, et al. (1987) Myosin subfragment-1 is sufficient to move actin filaments in vitro. *Nature* 328(6130):536–539.
27. McDonald HB, Stewart RJ, Goldstein LS (1990) The kinesin-like ncd protein of *Drosophila* is a minus end-directed microtubule motor. *Cell* 63(6):1159–1165.
28. Walker RA, Salmon ED, Endow SA (1990) The *Drosophila* claret segregation protein is a minus-end directed motor molecule. *Nature* 347(6295):780–782.
29. Ray S, Meyhöfer E, Milligan RA, Howard J (1993) Kinesin follows the microtubule's protofilament axis. *J Cell Biol* 121(5):1083–1093.
30. Bormuth V, et al. (2012) The highly processive kinesin-8, Kip3, switches microtubule protofilaments with a bias toward the left. *Biophys J* 103(1):L4–L6.
31. Yajima J, Mizutani K, Nishizaka T (2008) A torque component present in mitotic kinesin Eg5 revealed by three-dimensional tracking. *Nat Struct Mol Biol* 15(10):1119–1121.
32. Yajima J, Cross RA (2005) A torque component in the kinesin-1 power stroke. *Nat Chem Biol* 1(6):338–341.
33. Kagami O, Kamiya R (1992) Translocation and rotation of microtubules caused by multiple species of *Chlamydomonas* inner-arm dynein. *J Cell Sci* 103:653–664.
34. Can S, Dewitt MA, Yildiz A (2014) Bidirectional helical motility of cytoplasmic dynein around microtubules. *eLife* 3:e03205.
35. Ali MY, et al. (2002) Myosin V is a left-handed spiral motor on the right-handed actin helix. *Nat Struct Biol* 9(6):464–467.
36. Beausang JF, Schroeder HW, 3rd, Nelson PC, Goldman YE (2008) Twirling of actin by myosins II and V observed via polarized TIRF in a modified gliding assay. *Biophys J* 95(12):5820–5831.
37. Nishizaka T, Yagi T, Tanaka Y, Ishiwata S (1993) Right-handed rotation of an actin filament in an in vitro motile system. *Nature* 361(6409):269–271.
38. Brunnbauer M, et al. (2012) Torque generation of kinesin motors is governed by the stability of the neck domain. *Mol Cell* 46(2):147–158.
39. Bugiel M, Böhl E, Schäffer E (2015) The Kinesin-8 Kip3 switches protofilaments in a sideward random walk asymmetrically biased by force. *Biophys J* 108(8):2019–2027.
40. Vilfan A (2009) Twirling motion of actin filaments in gliding assays with nonprocessive myosin motors. *Biophys J* 97(4):1130–1137.
41. Hyman AA, Chrétien D, Arnal I, Wade RH (1995) Structural changes accompanying GTP hydrolysis in microtubules: Information from a slowly hydrolyzable analogue guanylyl-(alpha,beta)-methylene-diphosphonate. *J Cell Biol* 128(1-2):117–125.
42. Nitzsche B, Ruhnnow F, Diez S (2008) Quantum-dot-assisted characterization of microtubule rotations during cargo transport. *Nat Nanotechnol* 3(9):552–556.
43. Leibler S, Huse DA (1993) Porters versus rowers: A unified stochastic model of motor proteins. *J Cell Biol* 121(6):1357–1368.
44. Foster KA, Mackey AT, Gilbert SP (2001) A mechanistic model for Ncd directionality. *J Biol Chem* 276(22):19259–19266.
45. Mackey AT, Gilbert SP (2000) Moving a microtubule may require two heads: A kinetic investigation of monomeric Ncd. *Biochemistry* 39(6):1346–1355.
46. Pechatnikova E, Taylor EW (1999) Kinetics processivity and the direction of motion of Ncd. *Biophys J* 77(2):1003–1016.
47. Pechatnikova E, Taylor EW (1997) Kinetic mechanism of monomeric non-claret disjunctional protein (Ncd) ATPase. *J Biol Chem* 272(49):30735–30740.
48. Crevel IMTC, Lockhart A, Cross RA (1996) Weak and strong states of kinesin and ncd. *J Mol Biol* 257(1):66–76.
49. Rosenfeld SS, Renner B, Correia JJ, Mayo MS, Cheung HC (1996) Equilibrium studies of kinesin-nucleotide intermediates. *J Biol Chem* 271(16):9473–9482.
50. Furuta K, Toyoshima YY (2008) Minus-end-directed motor Ncd exhibits processive movement that is enhanced by microtubule bundling in vitro. *Curr Biol* 18(2):152–157.
51. Lockhart A, Crevel IM, Cross RA (1995) Kinesin and ncd bind through a single head to microtubules and compete for a shared MT binding site. *J Mol Biol* 249(4):763–771.
52. Foster KA, Correia JJ, Gilbert SP (1998) Equilibrium binding studies of non-claret disjunctional protein (Ncd) reveal cooperative interactions between the motor domains. *J Biol Chem* 273(52):35307–35318.
53. Howard J (1997) Molecular motors: Structural adaptations to cellular functions. *Nature* 389(6651):561–567.
54. Vilfan A (2014) Ensemble velocity of non-processive molecular motors with multiple chemical states. *Interface Focus* 4(6):20140032.
55. deCastro MJ, Ho CH, Stewart RJ (1999) Motility of dimeric ncd on a metal-chelating surfactant: Evidence that ncd is not processive. *Biochemistry* 38(16):5076–5081.
56. Song H, Endow SA (1997) Rapid purification of microtubule motor domain proteins expressed in bacteria. *Biotechniques* 22(1):82–85.
57. Nitzsche B, et al. (2010) Studying kinesin motors by optical 3D-nanometry in gliding motility assays. *Methods Cell Biol* 95:247–271.
58. Gell C, et al. (2010) Microtubule dynamics reconstituted in vitro and imaged by single-molecule fluorescence microscopy. *Methods Cell Biol* 95:221–245.
59. Ruhnnow F, Zwicker D, Diez S (2011) Tracking single particles and elongated filaments with nanometer precision. *Biophys J* 100(11):2820–2828.

Supporting Information

Nitzsche et al. 10.1073/pnas.1525313113

Correlation Functions

We calculated the correlation functions as

$$C_{II}(\Delta x) = \frac{\langle \Delta I(x) \Delta I(x + \Delta x) \rangle}{\langle (\Delta I(x))^2 \rangle} \quad [\text{S1}]$$

$$C_{yy}(\Delta x) = \frac{\langle y(x) y(x + \Delta x) \rangle}{\langle (y(x))^2 \rangle} \quad [\text{S2}]$$

and the cross-correlation function as

$$C_{yI}(\Delta x) = \frac{\langle y(x) \Delta I(x + \Delta x) \rangle}{\sqrt{\langle (y(x))^2 \rangle \langle (\Delta I(x))^2 \rangle}}. \quad [\text{S3}]$$

Here $\Delta I(x)$ denotes the deviation from the average intensity of that trajectory as a function of the longitudinal distance traveled. It serves as a measure for the vertical displacement $z(x)$. $y(x)$ denotes the lateral deviation, which has $\langle y \rangle = 0$ by definition. The correlation functions from datasets that are shown in Fig. 1 for three ATP concentrations are evaluated in Fig. S1. The cross-correlation function clearly shows a 90° phase shift between the lateral distance and the intensity (vertical position), which is indicative of right-handed helical rotation (clockwise as seen in the direction of motion).

Distribution of States After Strong Binding

Here we discuss a more general model in which the motor passes through N states between initial strong binding and detachment. The transitions between the states are assumed to be irreversible and the mean dwell time in state i is τ_i . The probability that the motor is found in state i at time t after initial strong binding is illustrated in Fig. S3. The average lever arm position among all bound motors (a generalization of Eq. 2) is

$$\langle \xi \rangle = \frac{\sum_{i=1}^N \sum_{j=i}^N d_i \tau_j}{\sum_{i=1}^N \tau_i}. \quad [\text{S4}]$$

The average microtubule displacement after binding (which generalizes Eq. 5) then reads

$$\langle x \rangle = v \frac{\sum_{i=1}^N \sum_{j=i}^i \tau_i \tau_j}{\sum_{i=1}^N \tau_i}. \quad [\text{S5}]$$

One can use these equations to derive the velocity and angular velocity as a function of [ATP], but the generalization to N states leads to no improvement in the fit quality over the two-state model.

Alternative Solution

In the following we derive the probability densities as a function of strain for the two-state model. The derivation represents an alternative to the distributions shown in the main text, which are function of time since initial binding. Let $P_0(t)$ denote the probability that a motor is in the detached state, $P_1(x, t)$ the probability density that it is in state 1, with its root at distance x from the MT binding site, and $P_2(x, t)$ the equivalent probability density for state 2. For a filament gliding with velocity v leading with its + end, the dynamics of the system is given by the following set of master equations:

$$\left(\frac{\partial}{\partial t} + v \frac{\partial}{\partial x} \right) P_1(x, t) = \frac{1}{\tau_{\text{off}}} P_0(t) \Phi(x) - \frac{1}{\tau_1} P_1(x, t) \quad [\text{S6}]$$

$$\left(\frac{\partial}{\partial t} + v \frac{\partial}{\partial x} \right) P_2(x, t) = \frac{1}{\tau_1} P_1(x, t) - \frac{1}{\tau_2} P_2(x, t) \quad [\text{S7}]$$

$$\frac{\partial}{\partial t} P_0(t) = \frac{1}{\tau_2} \int_{-\infty}^{\infty} P_2(x, t) dx - \frac{1}{\tau_{\text{off}}} P_0(t) \quad [\text{S8}]$$

together with the normalization condition

$$P_0(t) + \int_{-\infty}^{\infty} (P_1(x, t) + P_2(x, t)) dx = 1. \quad [\text{S9}]$$

$\Phi(x)$, also normalized to 1, denotes the distribution of strains at the time of attachment, which we set as $\Phi(x) = \sqrt{K/2\pi k_B T} \exp(-Kx^2/2k_B T)$, but its exact form is not relevant for our derivation as long as its mean is zero, $\int_{-\infty}^{\infty} \Phi(x) x dx = 0$.

In the stationary state, we set $\partial P_0 / \partial t = \partial P_1 / \partial t = \partial P_2 / \partial t = 0$ and obtain the formal solution

$$P_1(x) = \mathcal{N} \int_{-\infty}^{\infty} \frac{1}{v} \exp\left(-\frac{x-x'}{\tau_1 v}\right) \theta(x-x') \Phi(x') dx' \quad [\text{S10}]$$

$$P_2(x) = \mathcal{N} \int_{-\infty}^{\infty} \frac{\tau_2}{v(\tau_1 - \tau_2)} \left(\exp\left(-\frac{x-x'}{\tau_1 v}\right) - \exp\left(-\frac{x-x'}{\tau_2 v}\right) \right) \theta(x-x') \Phi(x') dx' \quad [\text{S11}]$$

$$P_0 = \mathcal{N} \tau_{\text{off}} \quad [\text{S12}]$$

with $\mathcal{N} = 1/(\tau_1 + \tau_2 + \tau_{\text{off}})$. Two examples of the distributions are shown in Fig. S5. The strain on the elastic element is $d_1 - x$ in state 1 and $d_1 + d_2 - x$ in state 2. The average force per motor can therefore be calculated as

$$\frac{F}{N} = \int_{-\infty}^{\infty} (P_1(x) K(d_1 - x) + P_2(x) K(d_1 + d_2 - x)) dx. \quad [\text{S13}]$$

From Eqs. S10 and S11 we obtain the integrals

$$\int_{-\infty}^{\infty} P_1(x) dx = \mathcal{N} \tau_1 \quad \int_{-\infty}^{\infty} P_1(x) x dx = \mathcal{N} \tau_1^2 v \quad [\text{S14}]$$

$$\int_{-\infty}^{\infty} P_2(x) dx = \mathcal{N} \tau_2 \quad \int_{-\infty}^{\infty} P_2(x) x dx = \mathcal{N} \tau_2 (\tau_1 + \tau_2) v \quad [\text{S15}]$$

and finally the force-velocity relationship

$$\frac{F}{N} = \mathcal{N} (d_1 \tau_1 + (d_1 + d_2) \tau_2 - (\tau_1^2 + \tau_1 \tau_2 + \tau_2^2) v). \quad [\text{S16}]$$

The unloaded velocity ($F = 0$) is given by

$$v = \frac{d_1 \tau_1 + (d_1 + d_2) \tau_2}{\tau_1^2 + (\tau_1 + \tau_2) \tau_2}, \quad [\text{S17}]$$

confirming Eq. 6 in the main text.

Monte-Carlo Simulation

We further validated the model solution by comparing the velocity v (Eq. 6) and helical pitch λ (Eq. 12) to a Monte-Carlo simulation with the same parameters. In the simulation we randomly distributed the motors underneath the gliding microtubule with an average linear density $\rho = 10 \mu\text{m}^{-1}$. For the sake of simplicity we place all motors on one line (i.e., they have the same angular distribution at attachment). For the longitudinal and angular elasticity we use the values $K = 0.1 \text{ pN/nm}$ and $\gamma = 10 k_B T$, respectively. The kinetic transitions were simulated with the Gillespie algorithm. After each step the microtubule was instantaneously moved to achieve force and torque equilibrium. Fig. S2 shows the results for filament lengths covering on average $\langle N \rangle = \rho L = 20$ and 40 motors. In both cases the deviation from the steady-state analytical result is insignificant.

Model Taking into Account the Presence of ADP

Adding ADP to the solution can lead to the reversal of the initial weak-to-strong binding transition. The inverse transitions have to be incorporated into the model in a way that keeps it thermodynamically consistent, adhering to the principle of detailed balance. Therefore, a more detailed description of the angular distribution of attached motors is needed.

The rate of strong binding (ADP release) to various sites on a microtubule is proportional to the Boltzmann factor formed from the elastic distortion energy:

$$k_{-\text{ADP}}(\theta) \propto \exp\left(-\frac{\gamma\theta^2}{2k_B T}\right). \quad [\text{S18}]$$

Here θ denotes the azimuthal angle of an ncd head relative to its unstrained position (i.e., the angle by which the microtubule would need to be rotated to release the strain). γ represents the effective angular elasticity of the motor, akin to longitudinal elasticity K . After binding, the motor undergoes an off-axis stroke of δ_1 (measured about the microtubule axis) and the total angular strain on it (now in state 0) is $\theta + \delta_1$. At this point we neglect the microtubule rotation while the motor is bound, because it would only have a small effect.

The ADP binding with subsequent strong-to-weak transition is the reverse of the above transition. The principle of detailed balance states that

$$\frac{k_{-\text{ADP}}(\theta)}{k_{+\text{ADP}}(\theta)} \propto \exp\left(-\frac{\gamma(\theta + \delta_1)^2}{2k_B T}\right). \quad [\text{S19}]$$

For the angular dependence of the ADP binding rate it follows

$$k_{+\text{ADP}}(\theta) = k_{+\text{ADP}}^0 \exp\left(-\frac{\gamma(\theta^2 - (\theta + \delta_1)^2)}{2k_B T}\right). \quad [\text{S20}]$$

At any angle θ the state 0 exits either through ATP or ADP binding. The probability that a motor in this state has the angular strain $\theta + \delta_1$ is proportional to

$$P(\theta) \propto \frac{k_{-\text{ADP}}(\theta)}{k_{+\text{ATP}}[\text{ATP}] + k_{+\text{ADP}}(\theta)[\text{ADP}]}. \quad [\text{S21}]$$

From this equation we can determine the expectation value of the angle θ in state 0:

$$\theta_0 = \langle \theta \rangle = \frac{\int \theta P(\theta) d\theta}{\int P(\theta) d\theta}. \quad [\text{S22}]$$

θ_0 is a function of the ratio $[\text{ADP}]/[\text{ATP}]$. In two limiting cases its value is easy to understand intuitively: For $[\text{ADP}] = 0$ we have $\theta_0 = 0$, meaning that the average angular strain on the motors after attachment is δ_1 —we already assumed this in the main text. For $[\text{ATP}] = 0$ we have $\theta_0 = -\delta_1$ and the motors in state 0 have on average no angular strain. This limit describes the situation in which motors are in equilibrium and not capable of generating torque.

To obtain the corrected equations for λ and v we use the following considerations. (i) We replace the off-axis strain in the first bound state (δ_1) with $\theta_0 + \delta_1$. (ii) We replace Eq. 5 with

$$\langle x \rangle = v \frac{\tau_1^2 + R(\tau_1 + \tau_2)\tau_2}{\tau_1 + R\tau_2}, \quad [\text{S23}]$$

where τ_1 is the corrected dwell time in the first bound state, $\tau_1 = 1/(k_{+\text{ATP}}[\text{ATP}] + k_{+\text{ADP}}[\text{ADP}])$, and R is the probability that the first state exits through ATP rather than ADP binding,

$$R = \frac{k_{+\text{ATP}}[\text{ATP}]}{k_{+\text{ATP}}[\text{ATP}] + k_{+\text{ADP}}[\text{ADP}]}. \quad [\text{S24}]$$

The substitute for Eq. 11 becomes

$$\begin{aligned} \lambda &= 2\pi \frac{d_1\tau_1 + R(d_1 + d_2)\tau_2}{(\theta_0 + \delta_1)\tau_1 + R(\theta_0 + \delta_1 + \delta_2)\tau_2} \\ &= 2\pi \frac{\frac{d_1}{k_{+\text{ATP}}^0[\text{ATP}]} + \frac{d_1 + d_2}{k_{\text{det}}}}{\frac{\theta_0([\text{ADP}]/[\text{ATP}] + \delta_1)}{k_{+\text{ATP}}^0[\text{ATP}]} + \frac{\theta_0([\text{ADP}]/[\text{ATP}] + \delta_1 + \delta_2)}{k_{\text{det}}}}. \end{aligned} \quad [\text{S25}]$$

Because $\theta_0([\text{ADP}]/[\text{ATP}])$ has the opposite sign of δ_1 , added ADP generally leads to an increased pitch. The expression for velocity in the model with friction that replaces Eq. 10 reads

$$v = \frac{\frac{d_1}{k_{+\text{ATP}}^0[\text{ATP}]} + \frac{d_1 + d_2}{k_{\text{det}}} - \frac{f}{K} \left(\tau_{\text{off}} \left(1 + \frac{k_{+\text{ADP}}[\text{ADP}]}{k_{+\text{ATP}}[\text{ATP}]} \right) + \frac{1}{k_{+\text{ATP}}^0[\text{ATP}]} + \frac{1}{k_{\text{det}}} \right)}{\frac{1/k_{\text{det}} + 1/(k_{+\text{ATP}}^0[\text{ATP}])}{k_{+\text{ADP}}[\text{ADP}] + k_{+\text{ATP}}[\text{ATP}]} + \left(\frac{1}{k_{\text{det}}} \right)^2}. \quad [\text{S26}]$$

We used these equations to fit the data under the constraint $d_1 = 0$ (a finite d_1 brings no improvement in the quality of the fit). We globally fitted the velocity as a function of $[\text{ATP}]$, as well as pitch as a function of $[\text{ADP}]$ and $[\text{ATP}]$. In addition, we assumed the following values: $d_2 = 9 \text{ nm}$, $\tau_{\text{off}} \approx 0$, and $\gamma = 10 k_B T$ (the latter has a very weak influence on the result). The pitch as a function of $[\text{ADP}]$ is shown in Fig. S6A.

Fig. S6B shows the velocity as a function of the ADP concentration. Although the model predicts some increase in velocity with the addition of ADP, it cannot explain the strong increase at $75 \mu\text{M}$ ATP. A possible explanation is that ADP releases some of the inactive motors and therefore reduces friction. A reduction of the friction force by 30% could explain the increase.

Sensitivity Analysis

The model without friction and without ADP contains a single free parameter, namely the power stroke distance $d_1 + d_2$. It has no influence on the fit quality and other parameters scale proportionally δ_1 , $\delta_1 + \delta_2$, d_1 or inversely proportional (kinetic rates).

The model with friction additionally contains parameters d_1 (which could be fitted, but is too small to justify a fitting parameter), τ_{off} , and γ . Fig. S7 shows the dependence of fitting results, as well as the fit quality (χ^2) on these parameters.

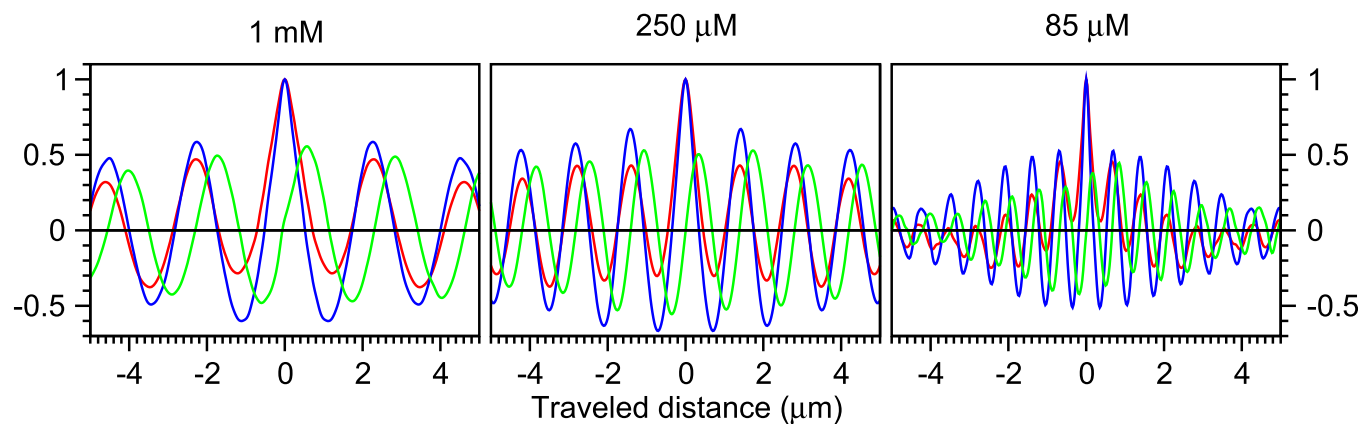


Fig. S1. Autocorrelation functions of FLIC intensity (C_{II} , red) and lateral displacement (C_{yy} , blue), and the cross-correlation function between intensity and lateral displacement (C_{yI} , green).

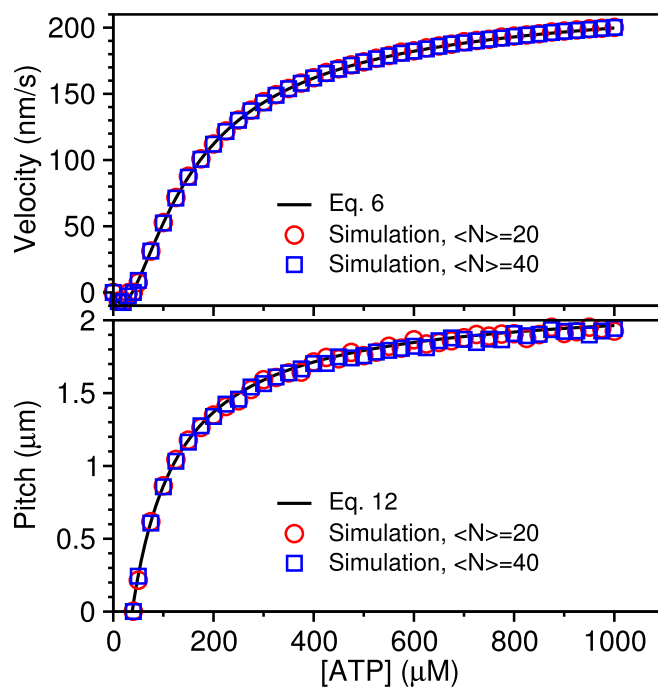


Fig. S2. Monte-Carlo simulation of the model without friction with parameters from Table 1, for filaments covering on average $\langle N \rangle = 20$ (red circles) and $\langle N \rangle = 40$ (blue squares). The continuous lines show the result of the analytical model.

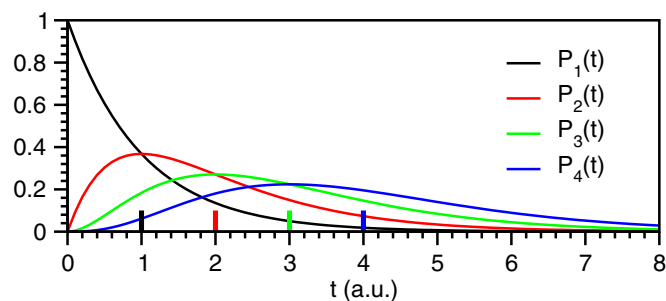


Fig. S3. A hypothetical system with four consecutive states with equal transition rates. The curves show the probability that the molecule is in state i at time t if it was in state 1 at time 0. The small bars denote the mean of each distribution.

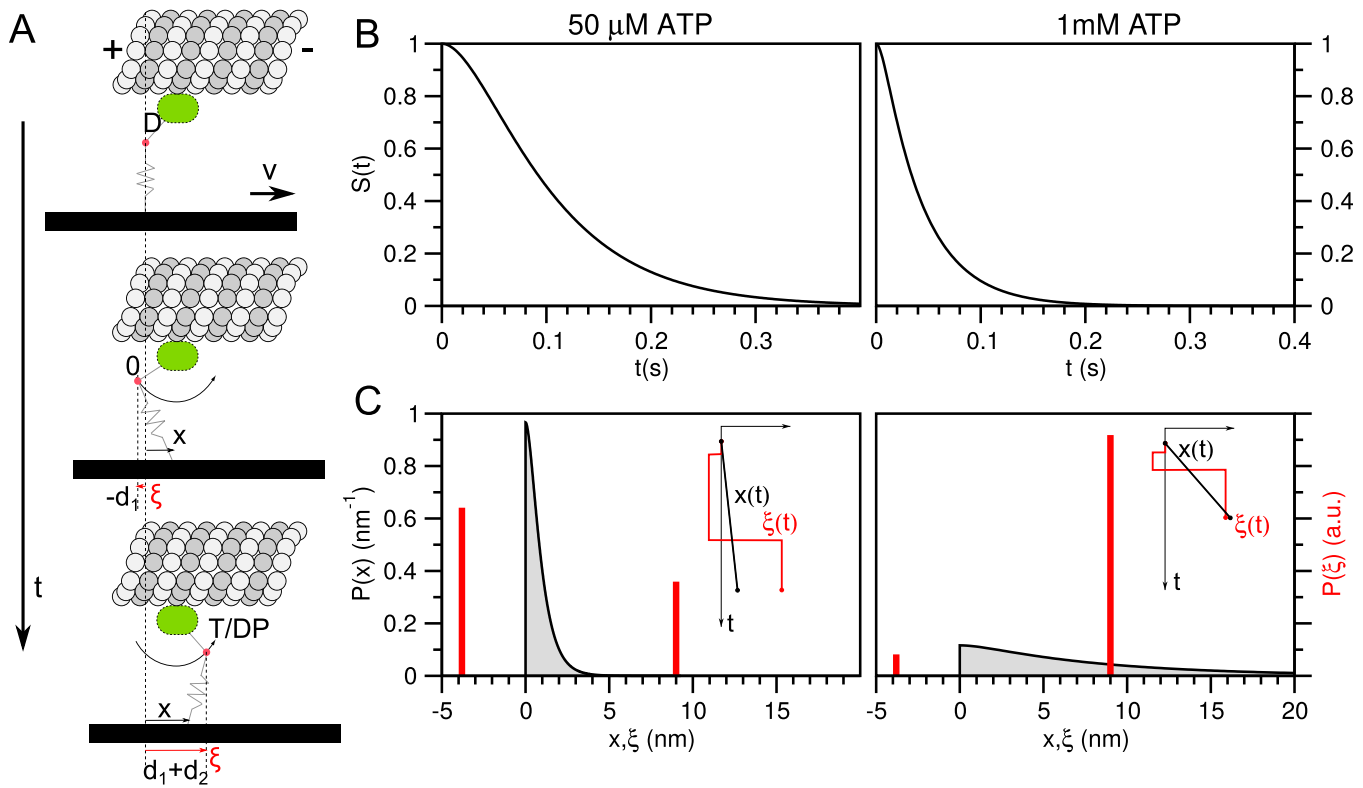


Fig. 54. Theoretical model. (A) Temporal sequence of substeps shown in a frame of reference that is comoving with the MT. ξ denotes the stalk displacement since initial binding and changes its value with each substep. $x = vt$ denotes the displacement of the gliding MT relative to the glass surface in the same period. (B) Survival function $S(t)$ (probability that a motor is still strongly bound at time t after the initial binding) for two different ATP concentrations. (C) Distributions of x (black) and ξ (red, discrete distribution). Examples of both distances as a function of time during a cycle are shown as insets. All parameters have the fitted values for the model without friction.

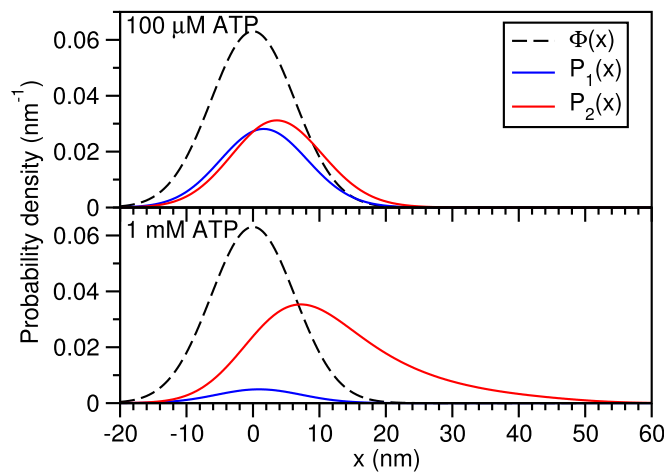


Fig. 55. Steady-state probability densities $P_1(x)$ and $P_2(x)$ as a function of the linear distance between the motor anchoring point and the microtubule binding site. Each distribution is calculated for unloaded sliding. The parameters correspond to the model without friction from the main text, and ATP concentrations are 100 μM (Top) and 1 mM (Bottom). $\Phi(x)$ shows the distribution of strains at the time of initial strong binding.

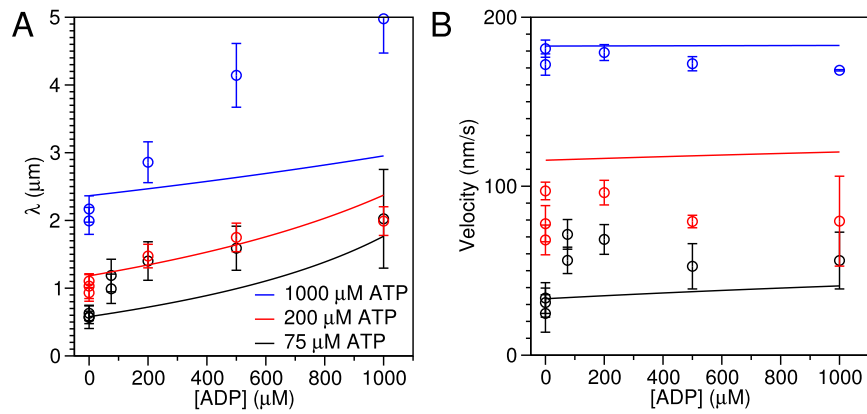


Fig. 56. (A) Global fit of the model with friction for all ATP and ADP concentrations. Pitch of MT rotation as a function of the ADP concentration. (B) Measured velocity as a function of the ADP concentration for 75 μM ATP (black), 200 μM ATP (red), and 1 mM ATP (blue). The continuous line shows the model prediction.

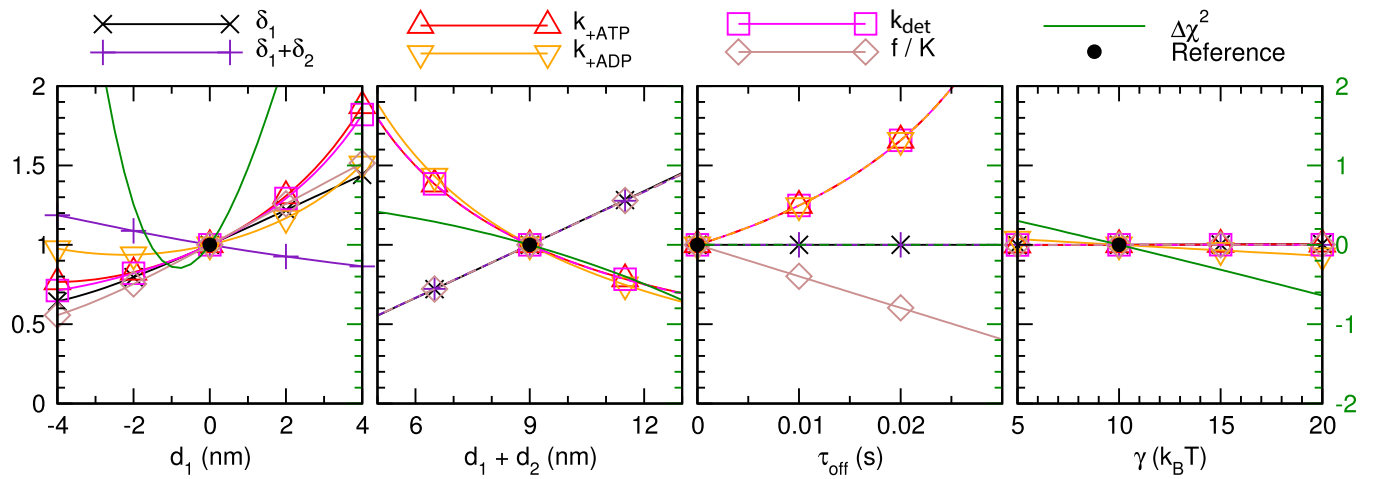


Fig. 57. Dependence of the relative values of the six fitted parameters (left scale) on the assumed values of d_1 , $d_1 + d_2$, τ_{off} , and γ . The green lines (right scale) show the difference in χ^2 .